Strong influence of climate change in uncharacteristic early spring heat in South America

Sarah Kew[1], Izidine Pinto[1], Lincoln Alves[2], Djacinto Santos[3], Renata Libonati[3], Sjoukje Philip[1], Mariam Zachariah[4], Clair Barnes[4], Joyce Kimutai[4], Maja Vahlberg[5], Julie Arrighi[5,6,7], Friederike Otto[4]

1. *Royal Netherlands Meteorological Institute (KNMI), De Bilt, The Netherlands*
2. *Instituto Nacional de Pesquisas Espaciais (INPE), São Paulo, Brazil*
3. *Universidade Federal do Rio de Janeiro (UFRJ), Rio de Janeiro, Brazil*
4. *Grantham Institute, Imperial College London, UK*
5. *Red Cross Red Crescent Climate Centre, The Hague, the Netherlands*
6. *Faculty of Geo-Information Science and Earth Observation (ITC), University of Twente, Enschede, the Netherlands*
7. *Global Disaster Preparedness Center, American Red Cross, Washington DC, USA*

Review authors

1. Ben Clark[4]
2. Joyce Kimutai[4]
3. Julie Arrighi[5,6,7]

Main findings

- While the full impacts of heatwaves remain unknown until months after the events, 4 casualties and many heat-related illnesses have been reported. Early spring extreme heat events often prove to be particularly impactful as local populations are not yet acclimatised to high temperatures. In addition, high population density, low vegetative cover and water-based spaces, high levels of air pollution, and inequality are additional risk drivers for mortality and morbidity within cities, rendering extreme heat particularly deadly for the urban poor.
- Using gridded observational products and observations the heat event as defined above is approximately a 1 in 30 year event in today's climate.
- While there is a high-level of confidence in the gridded products used to carry out the analysis, these do not capture very local records, many of which were broken during this heat episode. To incorporate these in future studies and inform early warning systems high quality and readily available weather station data is needed.
- To estimate the influence of human-caused climate change on this extreme heat we combine climate models with the observations.We find that because of human-induced climate change the event would have been 1.4 to 4.3 °C cooler had humans not warmed the planet by burning fossil fuels. Due to the strong trend the change in likelihood is not well defined: it has increased by at least 100 times.

- With future global warming, heat events like this will become even more common and hotter. At global mean temperatures of 2°C above pre-industrial levels, a heat event like this would be about another 5 times more likely and 1.1 to 1.6 °C hotter than today.
- Although ENSO may have influenced the large-scale weather patterns, the direct contribution to the extreme heat is small, compared to the climate change signal.
- While some losses will inevitably occur due to the extreme heat, in particular with respect to ecosystems it is misleading to assume that human impacts are inevitable. Adaptation to extreme heat can be effective at reducing morbidity and mortality. The authors were not able to identify any heat action plans that exist in the affected area, this leaves the potential for a window of opportunity to mitigate heat impacts on vulnerable people. Heat Action Plans that include early warning and early action, awareness raising and behaviour changing messaging, and supportive public services can reduce morbidity and mortality.

1 Introduction

During the months of August and September, the southern regions of Brazil and neighbouring countries endured an extended period of scorching temperatures, lasting for over 50 consecutive days. On the 15th September, the meteorological station in Balsas (7.455°S, 46.028°W) registered a peak temperature of 41.5°C (INMET, 2023). According to the Brazilian National Institute of Meteorology, INMET, the capital cities of Cuiabá (MT) and São Paulo (SP) experienced their warmest early spring in the past 63 years. The extreme heat began on 17th September across the center-south of the country, but after 24th September, the hot air mass prevailed in the center-north of the country, extending to the North and Northeast regions. The peak of the heat event occurred on 25th September, with anomalies of more than 7°C for the time of year in the southeast region, south of Bahia, east of Goiás and Mato Grosso do Sul, and the center-north of Paraná. Locally, in central and northern regions of the country, temperatures exceeded 40°C (Figure 1, INMET, 2023a).

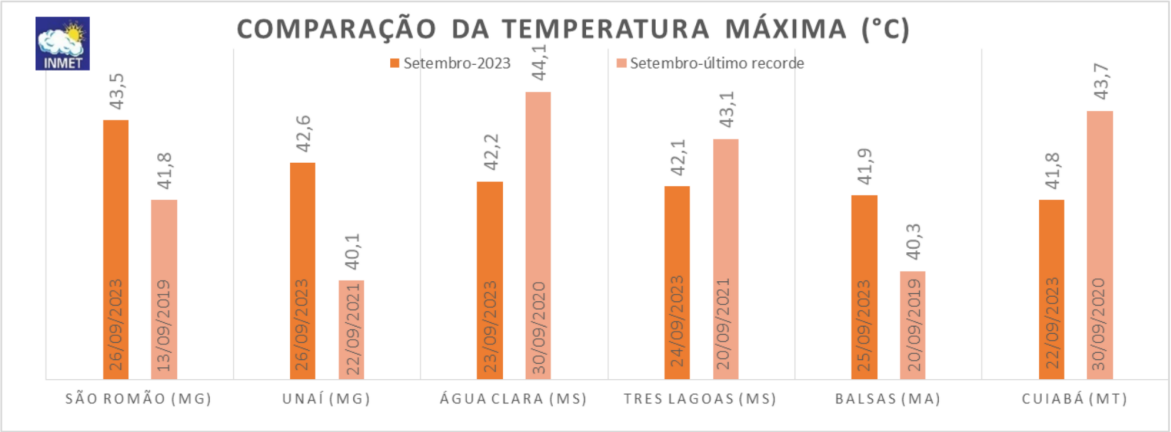

Figure 1. Comparison of the daily maximum temperature (°C) record between September 2023 (dark orange bars) and records of previous Septembers (light orange bars), for 6 locations in Brazil (source: INMET, 2023a).

Exceptional heat episodes were observed across much of Brazil during the winter months and early spring. Record-breaking temperatures exceeded historical average maximum values in all five regions, with temperatures nearing 40°C.

The hottest day ever recorded in São Paulo in September since data collection began in 1943 at the Mirante de Santana station (INMET) reached 37.1°C on September 30, 2020. This marks the second-highest maximum temperature in the historical series, only surpassed by the 37.8°C recorded on October 17, 2014. Other extremely hot days in the Mirante de Santana station's records, located in the northern zone of the city and managed by the National Institute of Meteorology, include 37.0°C on January 20, 1999, 36.7°C on January 19, 1999, and also 36.7°C on January 21, 1999.

In the state of São Paulo, the climatic conditions were similar to those observed between September and October 2020 when a heat dome settled in the region under an atmospheric blocking pattern with several days of extreme heat. A heat dome occurs with areas of high pressure that act as heat domes and have descending air (subsidence). This compresses the air at the surface and, through compression, heats the air column. In short, a heat dome is created when a high-pressure area remains over the same area for days or even weeks, trapping very hot air underneath like a lid on a pot. This heat dome was active between Paraguay and the Midwest and Southeast of Brazil. El Niño conditions continued to develop over the equatorial eastern Pacific and partially can contribute to new heat waves.

The extreme heat affected millions of people across Argentina, Brazil, Paraguay, and Bolivia. The full impact of heat events remains unknown until death certificates are collected or scientists can assess the number of excess fatalities, often weeks or months afterwards. However, four heat-related casualties have already been identified in São Paulo between August and September (Band Bora Brasil, 2023), and there are reports of increases in hospitalizations and outpatient care linked to exposure to the extreme heat (O Antagonista, 2023). Across the heat-affected countries, large wildfires are raging. At least 36 fires have been detected in Bolivia (País ED, 2023), 20 in Paraguay (ABC, 2023), and several more in Brazil, including in Bahia (The San Diego Union Tribune, 2023; CNN, 2023), Pantanal (O Globo, 2023), and the Amazon (France24, 2023).

A previous study by Dos Santos et al. (2015) investigated the impact of intense heat on mortality rates for the February 2014 heat in São Paulo. The analysis identified a critical 12-day period in February 2014 with temperatures consistently above 33°C, low humidity, and high ozone levels. During this time, there were 743 deaths, predominantly among individuals aged 60+, with specific causes such as nervous system diseases, genitourinary system diseases, mental disorders, and circulatory system diseases being notably affected. This study underscores the relationship between extreme weather conditions and excess deaths and highlights the importance of addressing weather-related risks in large urban areas through public policy.

To assess the extent to which human-induced climate change has influenced the occurrence of extremely high temperatures in the region most affected by severe heat (as illustrated in Fig. 2), we opted to examine the 2-metre land surface temperatures in the region that stretches from São Paulo near the East Coast of Brazil, to Paraguay. This region, which climatologically is relatively homogeneous, had the highest positive temperature anomalies in the September period, and includes the states (with the exception of Pará, in the north) where red alerts for heat were issued. Therefore we use a rectangular box over 11°S-28°S, 41°W-63°W for the spatial definition. As impacts were highest on a time scale of 1 to 2 weeks, we use the annual maximum of the 10-day average of daily maximum temperatures during August and September only (Aug-SepTX10x). Fig. 2 illustrates this

10-day measure for 2023, which is 17th to 26th September 2023 in three observational datasets, ERA5, CPC and MSWX.

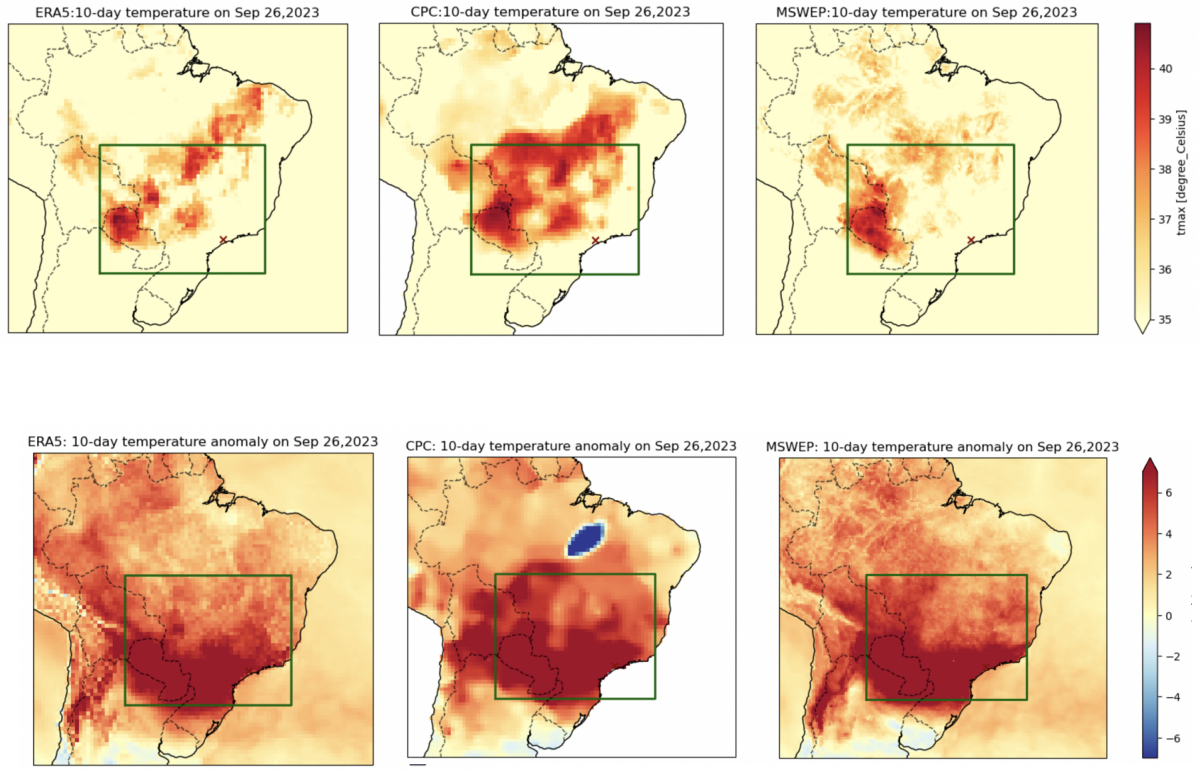

Figure 2. Top: ERA5, CPC and MSWX near surface temperature (T2m) [℃] showing 10-day average of daily maximum T2m for the period of 17th to 26th September 2023. The green outline represents the study region [11°S-28°S, 41°W-63°W]. Bottom: same as top row, as anomalies w.r.t. 1980-2010. See the note at the end of Section 3.1 concerning the CPC negative anomaly.

The Intergovernmental Panel on Climate Change's (IPCC) Sixth Assessment Report (AR6) states that it is virtually certain that the duration, frequency and intensity of hot extreme events at global scale, such as heatwaves, are increasing due to human activity (IPCC 2021; Seneviratne et al. 2021). Across many South American regions, mean temperature and extremely warm maximum and minimum temperatures have shown an increasing trend in the past (Gutiérrez et al. 2021), with high confidence that human-induced climate change is the main driver of these changes (Seneviratne et al. 2021, Fig SPM.3). In South America, this warming trend reached up to 1°C per decade during the period from 1975 to 2004 (de Barros Soares et al. 2017). This trend is expected to persist even under a scenario of 1.5°C global warming. For example, an extreme event such as a heatwave of an intensity that occurs once every 10 years could occur up to four times more frequently in a 1.5°C global warming scenario. That there is an increase in these events is considered virtually certain under a scenario of 4°C global warming. (Refer to Table 11.13 in Seneviratne et al., 2021 and Table 12.6 in Ranasinghe et al., 2021). While there are numerous studies on heatwaves in the Northern Hemisphere and their impacts, the Southern Hemisphere, particularly Brazil, lacks similar analyses despite its vast size and population. Geirinhas et al. (2018) investigated heatwaves in six major Brazilian cities and their associated climatic patterns over the past five decades. The findings revealed that heatwave frequency has significantly increased since the 1980s, particularly in São Paulo, Manaus, and Recife. Brasília has consistently experienced the highest number of heatwave days per year, while Rio de Janeiro has

recorded the lowest. Additionally, other studies have demonstrated an increased occurrence of heatwaves in South America during the period from August to October (Bitencourt et al., 2016; Ceccherini et al., 2016). Moreover, climate model projections suggest the intensification of temperature extremes in the coming decades (Feron et al., 2019).

A study by Miranda et al. (2023) addresses the growing concern of increasing extreme heat events in South America and their implications for public health. Despite the rising frequency of such events, there has been a lack of understanding regarding the large-scale, long-term variability, and trends of thermal stress in the continent. The study focused on analysing consecutive heat stress hours using the Universal Thermal Climate Index (UTCI) based on the ERA5-HEAT reanalysis. They considered the Köppen–Geiger climate classification and examined 31 of the most populous cities in South America. The results revealed distinct patterns, including an inland/coastline contrast and a noticeable northward increase in the number of hours under heat stress. Hotspots of heat stress were concentrated primarily around the Amazon, northern, and central regions of South America, with a significant portion (26–35%) of hours between 1979 and 2020 experiencing strong heat stress. Over the four decades studied, there was a significant increase in the annual number of hours characterised by heat stress. The rate of increase varied depending on the Köppen–Geiger climate class, ranging from +1.16 hours per year to +8.25 hours per year. Notably, the past two decades (2000 onwards) exhibited not only more consecutive hours of heat stress than the preceding two decades but also a higher persistence of such conditions.
The review by Libonati et al. (2022) addresses the significant impact of climate change on Brazil, particularly in terms of the increasing frequency, duration, and severity of compound drought-heatwave (CDHW) episodes. The review provides a synthesis of the evolving understanding of CDHW patterns in Brazil, with a focus on their impacts on fire occurrence and public health. It emphasises that heatwaves and droughts are becoming increasingly intertwined in several regions of Brazil, including the northeast, southeast, Amazonia, and the Pantanal. The review also highlights the correlation between CDHW events and heightened fire activity in Brazil over the past few decades, citing the catastrophic 2020 fires in the Pantanal as a recent example. Additionally, the study reveals that heatwaves have been linked to increased mortality and preterm births during record-breaking droughts in southeastern Brazil.

Valverde et al. (2023) conducted a comprehensive study on heatwaves in São Paulo State, Brazil, between 2000 and 2020, aiming to characterise their intensity, duration, spatial distribution, and atmospheric drivers. Their findings reveal varying levels of thermal stress across the state, with the north and northwest regions experiencing the highest average maximum temperatures (up to 38°C). The study identified an average heatwave temperature of 34.9°C, lasting around 5.3 days, with a significant increase in heatwave frequency between 2010 and 2020. Notably, 2015, 2016, and 2019 witnessed more heatwave events, primarily during the austral summer and spring. The research also highlighted key atmospheric characteristics associated with heatwaves, including anomalous anticyclonic circulation, thermal lows, Rossby wave patterns, and SST anomalies, suggesting a coupling between these oceanic and atmospheric factors as triggers for heatwave events, providing crucial insights for climate monitoring and adaptation strategies in the region.

2 Data and methods

2.1 Observational data

In this study, we investigated three gridded observational dataset. The first is the NOAA Climate Prediction Center (CPC) daily maximum temperature dataset. This is a gridded product from NOAA PSL, Boulder, Colorado, USA known as the CPC Global Unified Daily Gridded data. It is available at 0.5° x 0.5° resolution, for the period 1979-present (Chen et al., 2008). Data are available from NOAA. This dataset has been subjected to extensive quality assessments in previous studies, which showed that the dataset reproduces the temperature variability adequately over South America.

As a second dataset used is the Multi-Source Weather (MSWX) v2.8 dataset (updated from Beck et al., 2019), a fully global product, available at 3-hourly intervals and at 0.1° spatial resolution, available from 1979 to present This product combines gauge-, satellite-, and reanalysis-based data.

The third dataset is the European Centre for Medium-Range Weather Forecasts (ECMWF) reanalysis product ERA5, which begins in the year 1950 (Hersbach et al., 2020). We use daily maximum temperature data from this product. It should be noted that the variables from ERA5 are not directly assimilated, but these are generated by atmospheric components of the Integrated Forecast System (IFS) modelling system.
The re-analysis is available until the end of the preceding month (August 2023). We extend the re-analysis data with the ECMWF analysis (up to 27 September 2023) to cover the period of the event.

We also analyse daily maximum temperatures in São Paulo, measured at the Mirante de Santana station from 1961 to 2023, obtained from the INMET.

As a measure of anthropogenic climate change we use the (low-pass filtered) global mean surface temperature (GMST), where GMST is taken from the National Aeronautics and Space Administration (NASA) Goddard Institute for Space Science (GISS) surface temperature analysis (GISTEMP, Hansen et al., 2010 and Lenssen et al. 2019).

2.2 Model and experiment descriptions

We use three multi-model ensembles from climate modelling experiments using very different framings (Philip et al., 2020): Sea Surface temperature (SST) driven global circulation high resolution models, coupled global circulation models and regional climate models.

1. Coordinated Regional Climate Downscaling Experiment CORDEX-CORE (10 models with at 0.44° resolution (SAM-44) and 3 models at 0.22° resolution (SAM-22)) multi-model ensemble (Gutowski et al., 2016; Giorgi et al., 2021), comprising 13 simulations resulting from pairings of Global Climate Models (GCMs) and Regional Climate Models (RCMs)). These simulations are composed of historical simulations up to 2005, and extended to the year 2100 using the RCP8.5 scenario.

2. CMIP6. This consists of simulations from 20 participating models with varying resolutions. For more details on CMIP6, please see Eyring et al., (2016). For all simulations, the period 1850 to 2015

is based on historical simulations, while the SSP5-8.5 scenario is used for the remainder of the 21st century.

3. HighResMIP SST-forced model ensemble (Haarsma et al. 2016), the simulations for which span from 1950 to 2050. The SST and sea ice forcings for the period 1950-2014 are obtained from the 0.25° x 0.25° Hadley Centre Global Sea Ice and Sea Surface Temperature dataset that have undergone area-weighted regridding to match the climate model resolution. For the 'future' time period (2015-2050), SST/sea-ice data are derived from RCP8.5 (CMIP5) data, and combined with greenhouse gas forcings from SSP5-8.5 (CMIP6) simulations (see Section 3.3 of Haarsma et al. 2016 for further details).

2.3 Statistical methods

In this study we analyse time series from a longitude-latitude box over Southern Brazil and Paraguay - 11°S-28°S, 41°W-63°W of Aug-Sep 10-day average maximum temperature values. Methods for observational and model analysis, and for model evaluation and synthesis are used according to the World Weather Attribution Protocol, described in Philip et al. (2020), with supporting details found in van Oldenborgh et al. (2021), Ciavarella et al. (2021) and here.

The analysis steps include: (i) trend calculation from observations; (ii) model evaluation; (iii) multi-method multi-model attribution and (iv) synthesis of the attribution statement.
We calculate the return periods, Probability Ratio (PR; the factor-change in the event's probability) and change in intensity of the event under study in order to compare the climate of now and the climate of the past, defined respectively by the GMST values of now and of the preindustrial past (1850-1900, based on the Global Warming Index). To statistically model the event under study, we use a generalised extreme value (GEV) distribution that shifts with GMST. Next, results from observations and models that pass the evaluation tests are synthesized into a single attribution statement.

3 Observational analysis: return period and trend

3.1 Assessment of gridded datasets

To select the best available dataset for this study, we evaluate the gridded datasets as follows. We compare maps obtained from the three gridded observational datasets described in Section 2.1 with maps of daily maximum temperature anomalies (see Appendix) produced by INMET (Brazilian National Institute of Meteorology) based on an extended network of automatic and conventional weather stations since the year 1961. The INMET maps are available from the institution's website.
However, with only visual inspection of daily anomalies, it is difficult to distinguish which dataset performs best. On analysing the annual Aug-SepTX10x time series we found ERA5 to underestimate the event value (see Figure 3) compared to the other datasets. Furthermore, the years 1950-1970 exhibit odd spikes with much higher variability. Therefore we use ERA5 data starting from 1970, and the full length of the other datasets, which start in 1979.
We found ERA5 to be more weakly correlated to the other two datasets (CPC and ERA5; 0.814 and MSWX and ERA5; 0.791) than the correlation observed between the other two datasets (MSWX and

CPC: 0.976). Additionally we note that there is a strong negative anomaly in the CPC dataset visible in Figure 2 that is not present in the other two datasets. The reason for this is presently unclear, but being outside our study box, it is not included in the data analysed.

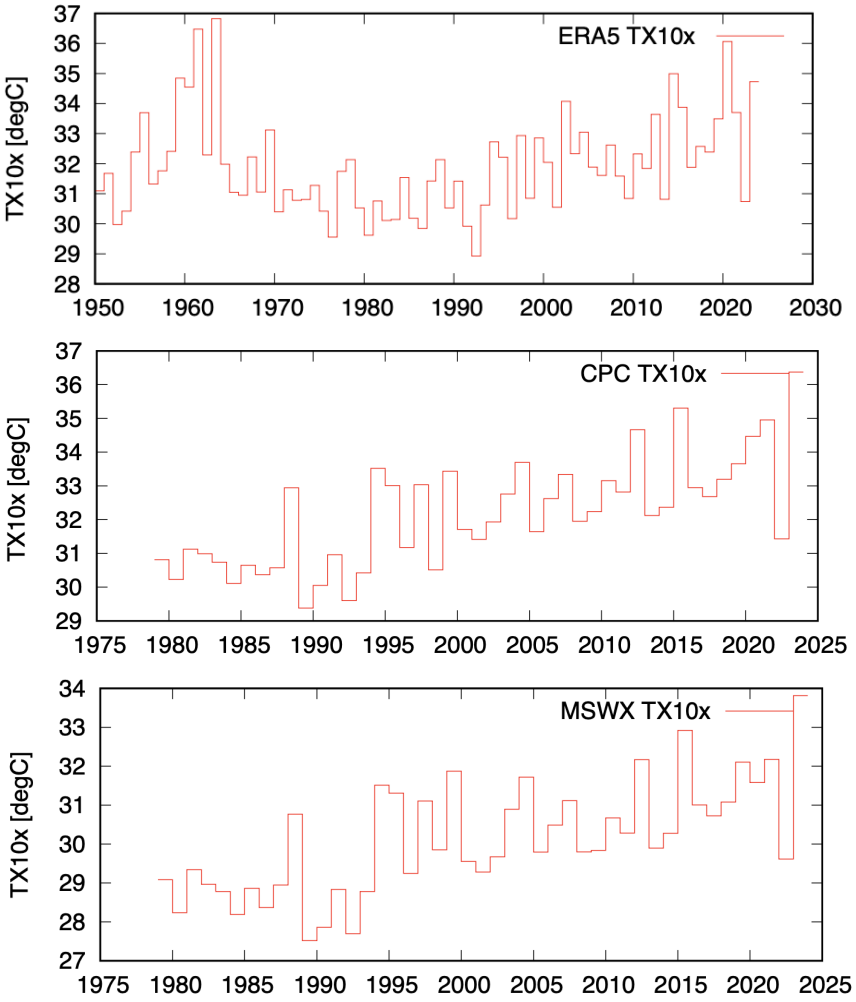

Figure 3. Time series of AugSepTX10x averaged over the study region for ERA5 (top), CPC (middle) and MSWX (bottom).

3.2 Analysis of gridded data

Using a GEV that shifts with the smoothed GMST, we calculate the return period, change in intensity and probability ratio between 2023 and a past climate that is 1.2 ℃ cooler than now (i.e. without anthropogenic warming). Figure 4 shows the results of these GEV fits applied to the ERA5, CPC and MSWX time series of Aug-SepTX10x over the study region. The left panels show Aug-SepTX10x as a function of the GMST anomaly, while the right panels show GEV return period curves for this variable in the present 2023 climate (red lines) and a hypothetical past climate when the global mean temperature was 1.2°C cooler (blue lines). All three datasets show a clear increase in frequency and intensity of hot events. The return period in the current climate in the CPC dataset is 52 years (15 to 882 years). The return period for ERA5 in the current climate is lower, as expected due to the relatively low value for the 2023 event, at 12 years (4.5 to 78 years). In the MSWX dataset, the return period estimate lies between the estimates from the other two datasets, with a best estimate of 34 years

(12 to 202 years). We choose to use a return period of 30 years for the model analysis, which lies in the range spanned by the three best estimates and is well within each of the datasets' uncertainty ranges.

These observational datasets indicate that the intensity, or magnitude, of such a 10-day event that happened in 2023 would have been much lower in the past. For instance, in CPC our analysis shows that the intensity would have been 4.9 ℃ (3.2 to 7.0 ℃) lower in the past, and 4.5 ℃ (3 to 6 ℃) in MSWX. For ERA5, the equivalent intensity change is smaller, at3.8 ℃ (1.9 to 5.1 ℃). The probability ratios are not well defined due to this strong trend, and such a hot event would have had a very low probability in the past. For CPC and MSWX we can only give a lower bound of the probability ratio between the current climate and a 1.2 ℃ cooler climate, which is respectively 44 or 31 times more likely. For ERA5 the best estimate is about fifteen thousand, with a lower bound of 7 times more likely. We therefore focus on the change in intensity rather than on the probability ratio.
The trend with respect to GMST in CPC and MSWX is higher than in ERA5. We note however that part of this difference is related to the different starting dates of the time series: if we use ERA5 over the same period as CPC, i.e. 1979-2023, the trend evaluates slightly higher and is therefore closer to the CPC trend. We choose to use all observational datasets analyses in the synthesis (see Section 6).

ERA 5

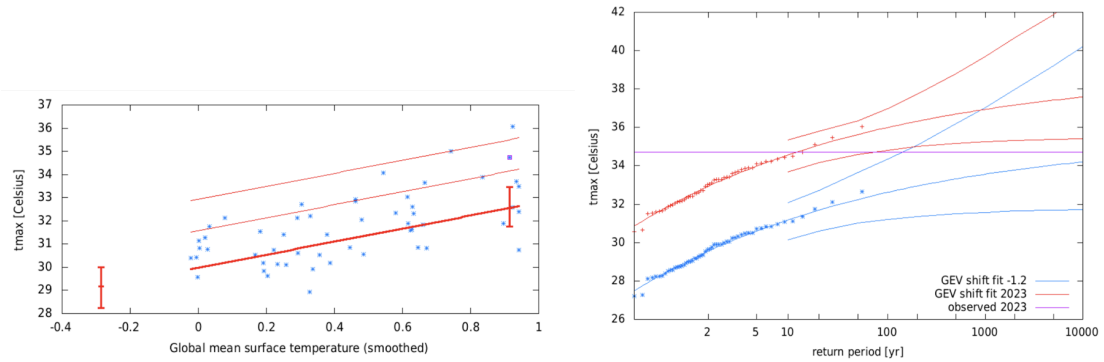

CPC

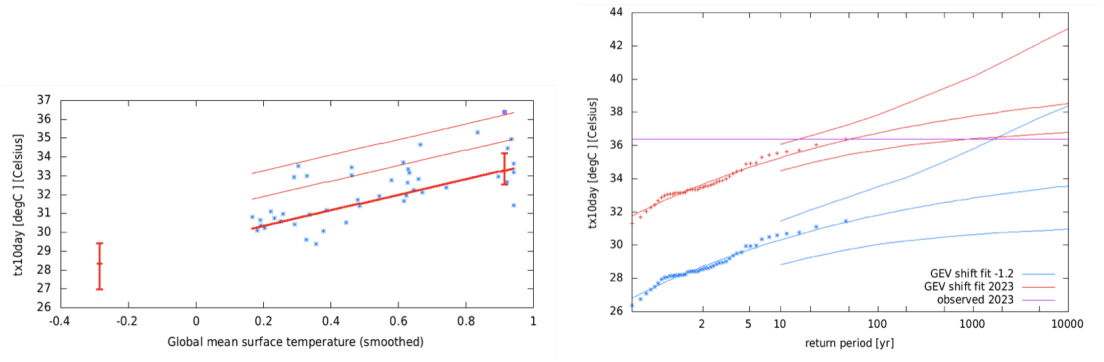

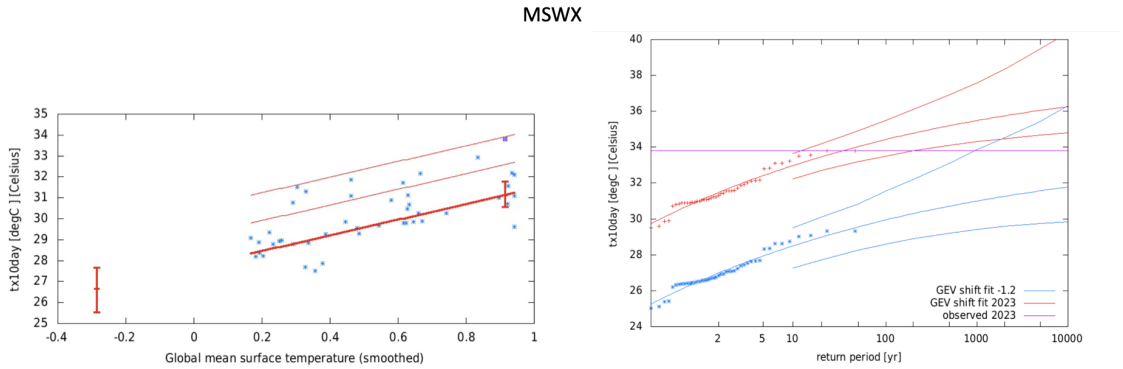

Figure 4. Fitted trends and return level plots for a non-stationary GEV fitted to AugSepTX10x. Left: Trend in annual maximum of AugSepTX10x as a function of the smoothed GMST from ERA5 (top), CPC (middle) and MSWX (bottom) records to change in global mean temperature. The thick red line denotes the time-varying mean, and the thin red lines show 1 standard deviation (s.d) and 2 s.d above. The vertical red lines show the 95% confidence interval for the location parameter, for the current, 2023 climate and the hypothetical, 1.2ºC cooler climate. The 2023 observation is highlighted with the magenta box. Right: Return periods for the 2023 climate (red lines) and the 1.2ºC cooler climate (blue lines with 95% CI), based on ERA5 data (top) and CPC (middle) and MSWX data (bottom).

3.3 Analysis of São Paulo station data

Station data for São Paulo are relatively complete for the years 1961-2023, except for the recent years 2020-2022, where all Aug-Sep values for 2020 are missing and some Aug-Sep values in 2021 and 2022. These missing data values may have an influence on the analysis. Furthermore, there are high values in the early years (see Figure 5), similar to the ERA5 data. Since we do not have information on homogeneity of the station data, we show only the extreme values fits in which we only use data from 1970 onwards, similar to ERA5, and we only report results for the whole dataset for comparison.

The return period in the current climate is 93 years (at least 123 years) based on the 1970-2023 data and 52 years (at least 16 years) using the entire dataset (1961-2023) . Similar to the gridded datasets, the station data indicate that the intensity, or magnitude, of a 10-day event of the same return period (rarity) as in 2023, would have been much lower in the past. Using data from 1970 onwards, such heat events are nowadays 4.6 ℃ (2.0 to 7.2 ℃) warmer than in a 1.2 ℃ cooler climate. This is 2.9 ℃ (1.0 to 5.1 ℃) for the whole dataset. The probability ratios are not well defined: at least 11 times more likely for the shorter series and 219 times (at least 3.9 times) more likely in the longer time series.

As a single station is not representative for the whole region, we cannot directly compare the station results to the results of the gridded datasets for the study area. Nevertheless, we note that the return period of the point location is somewhat higher than that in the gridded datasets, but the change in intensity is well within the estimates from the gridded datasets. The station series has been compared to ERA5 and CPC, analysed at the closest grid point to São Paulo (not shown). The gridded data sets generally follow the evolution of the São Paulo time series, with ERA5 showing a bias towards lower temperatures.

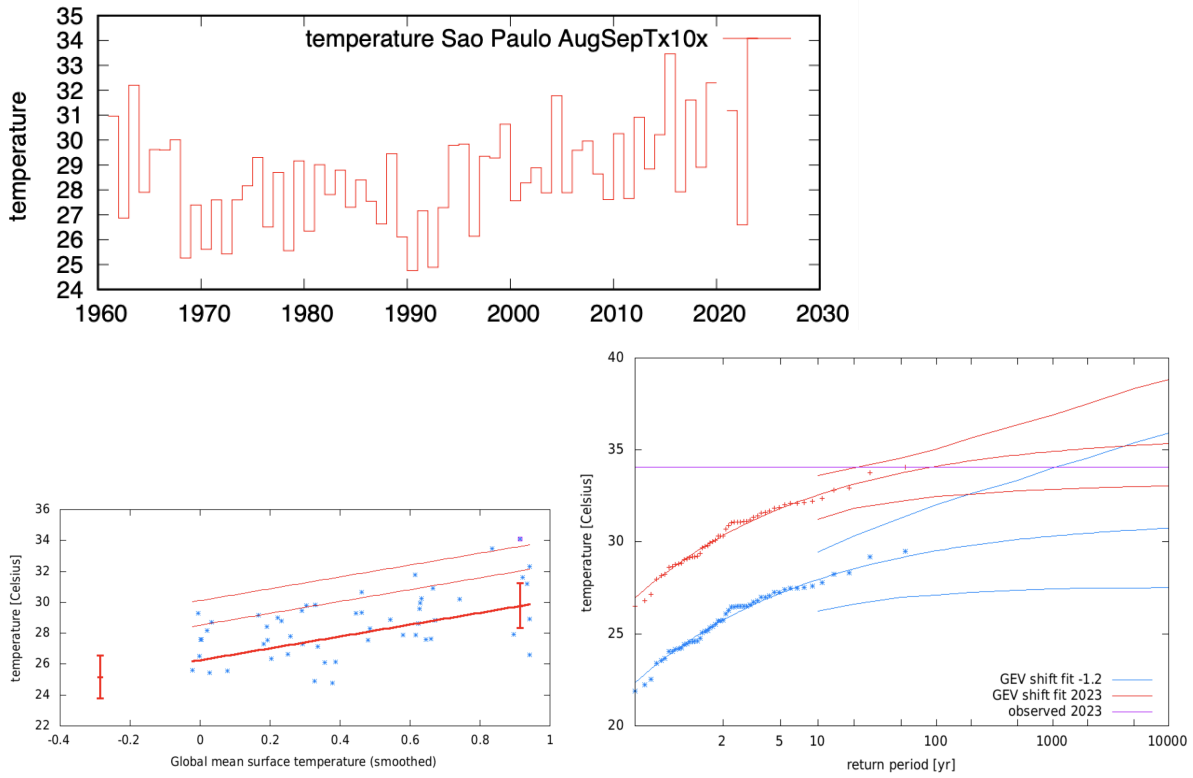

Figure 5. Time series of AugSepTX10x for the São Paulo station (top), and fitted trends and return level plots for a nonstationary GEV fitted to AugSepTX10x (bottom), similar to Figure XX3.

3.4 Influence of modes of natural variability

Although the correlation between the ENSO cycle and temperatures is visible in some months over parts of South America, the relation between ENSO and temperatures over our study region is weak for August and September (Figure 6). In fact, correlations between Niño3.4-rel (van Oldenborgh et al, 2021) and temperatures over the area are around zero at this time of year. The effect of including either September or August-September Niño3.4-rel as a covariate in the nonstationary model - similar to the analysis on the drought in East Africa - was checked using a likelihood ratio test and found not to improve the model enough to justify estimation of the extra parameter needed. Furthermore, when it was included, the effect of the Niño3.4-rel covariate was relatively small, increasing temperatures in the region by around 0.5°C in September 2023 (Figure 7): the effect of increasing GMST is much larger, as discussed above.

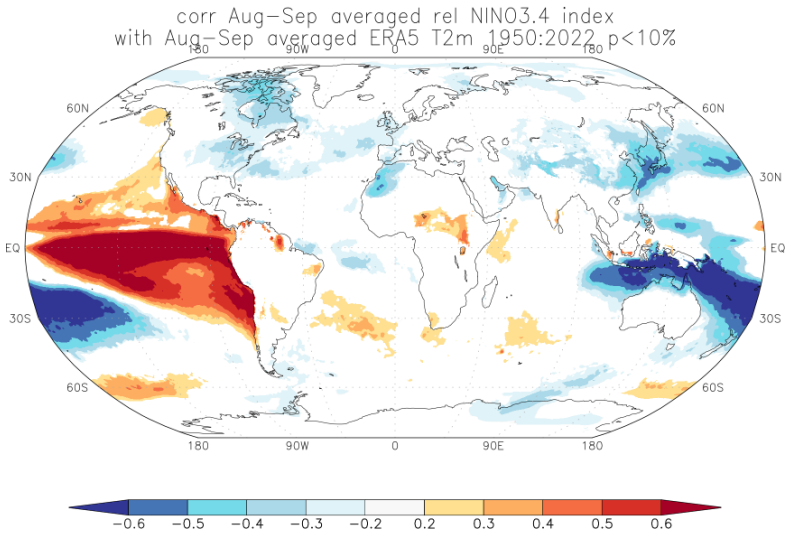

Figure 6: *ENSO-Temperature relationships for August-September, using data from ERA5. Blue colours indicate that, during El Niño, temperature is below average, red colours indicate higher temperatures during El Niño. As a measure of the strength of the relationship we used the correlation coefficient with the Niño3.4-rel index.*

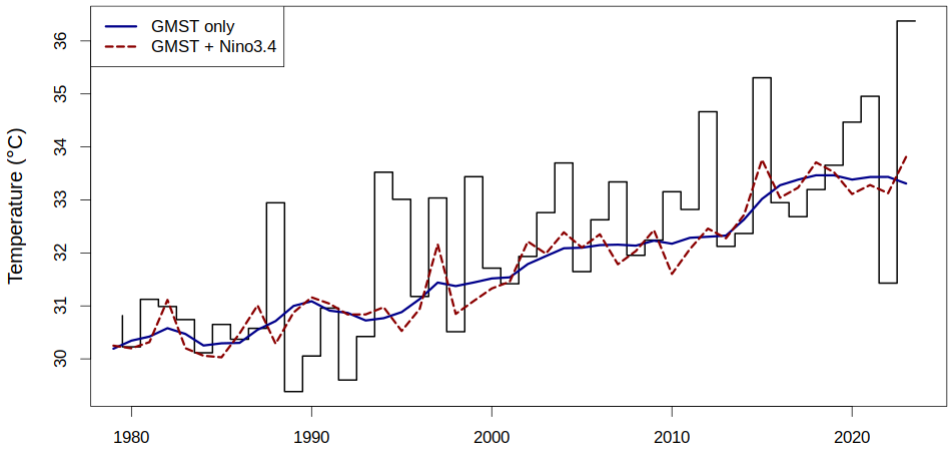

Figure 7: *CPC time series with nonstationary trend overlaid: dependent on GMST only (solid blue line) and dependent on GMST + Niño3.4-rel (dashed red line). Similar results were obtained using the other observational datasets.*

4 Model evaluation

In the subsections below we show the results of the model evaluation. Per multimodel ensemble (framing), WWA also uses models that only just pass the evaluation tests if there are only five models or less for that framing that perform well. This means that for CMIP6 we only use the models with label 'good', and for Cordex and HighResMIP we use models with labels 'good' and 'reasonable'. In addition, models for which the 1-in-30 yr event value differs from observations by around 5°C or more are excluded. Table 1 shows the model evaluation results. The climate models are evaluated against the observations in their ability to capture:

1. Seasonal cycles: For this, we qualitatively compare the model outputs against observations-based plots. We discard the models that exhibit multi-modality and/or ill-defined peaks in their seasonal cycles. We also discard the model if temperature seasonality varies significantly from the observations.

2. Spatial patterns: Models that do not match the observations in terms of the spatial patterns are excluded.

3. Parameters of the fitted GEV model. We discard the model if the model and observation parameters ranges do not overlap.

***Table 1**: Evaluation results for the climate models considered for the attribution analysis of Aug-SepTX10x in the study region. The table contains qualitative assessments of seasonal cycle and spatial pattern of precipitation from the models (good, reasonable, bad) along with estimates for dispersion parameter, and event magnitude. The corresponding estimates for the observational datasets are shown in blue. Based on overall suitability, the models are classified as good, reasonable or bad, shown by green, yellow and red highlights, respectively.*

Model / Observations	**Seasonal cycle**	**Spatial pattern**	**Sigma**	**Shape parameter**	**Event magnitude [˚C]**	**Conclusion**
CPC			1.03 (0.696 ... 1.24)	-0.15 (-0.31 ... 0.051)	36.376	
MSWX			0.949 (0.650 ... 1.12)	-0.13 (-0.25 ... 0.066)	33.81	
ERA5			1.08 (0.779 ... 1.26)	-0.17 (-0.38 ... 0.067)	34.725	
Model					**Threshold for 1-in-30 year event**	
ACCESS-CM2	good	good	1.40 (1.09 ... 1.59)	-0.25 (-0.43 ... -0.090)	34.97	reasonable
ACCESS-ESM1-5	good	bad	1.68 (1.24 ... 1.90)	-0.23 (-0.51 ... 0.090)	37.45	bad (spatial pattern)
CanESM5	bad	reasonable	1.21 (0.930 ... 1.39)	-0.17 (-0.35 ... 0.020)	42.78	bad seasonal cycle and very 1-in-30 yr event value
CMCC-ESM2	good	good	1.17 (0.840 ... 1.34)	-0.25 (-0.53 ... 0.010)	36.99	good
CNRM-CM6-1-HR	good	good	1.31 (0.860 ... 1.53)	-0.22 (-0.37 ... 0.10)	37.37	reasonable

CNRM-CM6-1	good	good	1.44 (1.06 ... 1.64)	-0.26 (-0.48 ... -0.040)	36.5	reasonable
EC-Earth3	good	good	1.11 (0.830 ... 1.33)	-0.030 (-0.23 ... 0.14)	37.16	good
EC-Earth3-Veg	good	reasonable	1.68 (1.21 ... 1.99)	-0.25 (-0.39 ... -0.070)	38.91	Two only just reasonables, therefore exclude
EC-Earth3-Veg-LR	good	good	1.52 (1.18 ... 1.76)	-0.15 (-0.36 ... 0.030)	37.08	reasonable
FGOALS-g3	good	reasonable	0.860 (0.630 ... 1.01)	-0.12 (-0.30 ... 0.040)	38.52	reasonable (spatial pattern)
INM-CM4-8	good	good	1.38 (0.940 ... 1.64)	-0.24 (-0.44 ... -0.03)	38.67	reasonable
INM-CM5-0	good	good	1.48 (1.12 ... 1.70)	-0.28 (-0.49 ... -0.060)	36.8	reasonable
IPSL-CM6A-LR	good	good	1.15 (0.820 ... 1.36)	-0.17 (-0.36 ... 0.030)	34.67	good
MIROC6	bad	reasonable	1.57 (1.23 ... 1.76)	-0.28 (-0.48 ... -0.040)	41.77	bad, seasonal cycle and very high 1-in-30 yr event value
MPI-ESM1-2-HR	good	good	1.11 (0.890 ... 1.27)	-0.23 (-0.42 ... -0.040)	32.22	good
MPI-ESM1-2-LR	good	reasonable	1.11 (0.800 ... 1.30)	-0.18 (-0.43 ... 0.090)	30.59	bad, very low 1-in-30 yr event value, therefore exclude
MRI-ESM2-0	good	good	1.71 (1.22 ... 2.01)	-0.10 (-0.28 ... 0.070)	37.31	reasonable, but only just, therefore exclude
NorESM2-LM	good	reasonable	1.06 (0.810 ... 1.23)	-0.14 (-0.32 ... 0.0)	35.62	reasonable
NorESM2-MM	good	good	1.18 (0.920 ... 1.33)	-0.25 (-0.44 ... -0.080)	34.49	good
TaiESM1	good	good	1.02 (0.780 ... 1.17)	-0.29 (-0.54 ... -0.040)	35.36	good
CNRM-CM6-1-HR	reasonable	good	1.12 (0.822 ... 1.41)	-0.13 (-0.48 ... 0.097)	37.722	reasonable
MPI-ESM1-2-HR	good	good	1.07 (0.809 ... 1.33)	-0.24 (-0.58 ... 0.0)	32.48	good
HadGEM3-	good	good	1.31 (0.922 ...	-0.25 (-0.58 ...	35.27	reasonable

GC31-MM			1.63)	0.077)		
CanESM2_r1_RCA4 historical-rcp85	good	good	1.03 (0.734 ... 1.49)	-0.32 (-1.1 ... -0.11)	35.112	good
CNRM-CM5_r1_RCA4 historical-rcp86	bad	good	1.23 (0.812 ... 1.63)	-0.13 (-0.50 ... 0.31)	34.798	bad
CSIRO-Mk3-6-0_r1_RCA4 historical-rcp87	reasonable	good	0.911 (0.643 ... 1.12)	-0.15 (-0.44 ... 0.24)	36.126	reasonable
EC-EARTH_r12_RCA4 historical-rcp88	bad	good	0.760 (0.580 ... 0.913)	-0.16 (-0.43 ... 0.049)	33.667	bad
GFDL-ESM2M_r1_RCA4 historical-rcp89	bad	good	1.04 (0.707 ... 1.33)	-0.31 (-1.1 ... -0.034)	35.009	bad
HadGEM2-ES_r1_RCA4 historical-rcp90	good	good	1.21 (0.855 ... 1.45)	-0.20 (-0.78 ... -0.0063)	33.987	good
IPSL-CM5A-MR_r1_RCA4 historical-rcp91	bad	good	0.949 (0.646 ... 1.26)	-0.21 (-0.60 ... 0.075)	37.269	bad
MIROC5_r1_RCA4 historical-rcp92	bad	good	1.04 (0.779 ... 1.43)	-0.14 (-1.0 ... 0.14)	35.884	bad
MPI-ESM-LR_r1_RCA4 historical-rcp93	reasonable	good	0.918 (0.713 ... 1.15)	-0.14 (-0.46 ... 0.085)	34.850	reasonable
MPI-ESM-LR_r1_REMO2009	good	good	0.987 (0.749 ... 1.23)	-0.089 (-1.0 ... 0.11)	36.206	good

historical-rcp 94						
HadGEM2-ES_r1_RegCM4-7 historical-rcp 85	reasonable	good	1.13 (0.767 ... 1.51)	-0.20 (-1.1 ... 0.25)	36.084	reasonable
MPI-ESM-MR_r1_RegCM4-7 historical-rcp 86 ()	bad (bimodal)	good	1.07 (0.807 ... 1.50)	-0.36 (-1.1 ... -0.12)	35.097	bad
NorESM1-M_r1_RegCM4-7 historical-rcp 87 ()	bad (bimodal)	good	0.919 (0.698 ... 1.19)	-0.34 (-1.0 ... -0.079)	35.290	bad

5 Multi-method multi-model attribution

This section shows Probability Ratios and change in intensity ΔI for models and also includes the values calculated from the fits with observations.

Table 2. *Probability ratio and change in intensity for models that passed the validation tests. Models that include runs for the future climate also include results for present vs future.*

	a. Past vs. present		**b. Present vs. future**	
Model / Observations	**Probability ratio PR [-]**	**Change in intensity ΔI [˚C]**	**Probability ratio PR [-]**	**Change in intensity ΔI [˚C]**
CPC	∞ (44 ... ∞)	4.9 (3.2 ... 7.0)		
MSWX	9.7e+9 (31 ... ∞)	4.5 (3.0 ... 6.1)		
ERA5	1.5e+4 (7.5 ... ∞)	3.4 (1.9 ... 5.1)		
CMCC-ESM2	6.6e+2 (19 ... 1.0e+4)	2.4 (1.6 ... 3.2)	6.4 (4.4 ... 23)	1.5 (1.3 ... 1.8)
EC-Earth3	20 (5.6 ... 1.0e+4)	1.9 (1.4 ... 2.5)	4.2 (3.0 ... 7.7)	1.3 (1.1 ... 1.6)
IPSL-CM6A-LR	2.4e+2 (7.9 ... 1.0e+4)	1.4 (0.80 ... 2.0)	4.7 (3.3 ... 11)	1.2 (0.98 ... 1.4)

MPI-ESM1-2-HR	28 (6.4 ... 1.0e+4)	2.8 (2.0 ... 3.6)	5.2 (3.4 ... 16)	1.6 (1.3 ... 1.9)
NorESM2-MM	5.2e+2 (5.0 ... 1.0e+4)	1.3 (0.46 ... 2.1)	6.7 (4.7 ... 13)	1.4 (1.1 ... 1.6)
TaiESM1	6.1e+3 (17 ... 1.0e+4)	1.8 (1.1 ... 2.6)	5.8 (4.0 ... 16)	1.5 (1.3 ... 1.7)
CNRM-CM6-1-HR	2.2e+2 (6.1 ... ∞)	2.0 (0.95 ... 3.0)		
MPI-ESM1-2-HR	2.8 (0.16 ... ∞)	0.48 (-0.66 ... 1.5)		
HadGEM3-GC31-MM	∞ (32 ... ∞)	2.7 (1.6 ... 3.7)		
CanESM2_r1_RCA4 historical-rcp85	6.8e+2 (4.6 ... ∞)	1.5 (0.82 ... 2.1)	4.9 (3.1 ... 17)	1.0 (0.82 ... 1.3)
CSIRO-Mk3-6-0_r1_RCA4 historical-rcp87	3.3e+3 (8.3 ... ∞)	2.4 (1.5 ... 3.4)	15 (8.1 ... 84)	1.5 (1.3 ... 1.8)
HadGEM2-ES_r1_RCA4 historical-rcp90	1.7e+2 (5.5 ... ∞)	1.5 (0.68 ... 2.3)	4.6 (3.2 ... 61)	1.1 (0.81 ... 1.3)
MPI-ESM-LR_r1_RCA4 historical-rcp93	3.2e+2 (6.6 ... ∞)	1.7 (1.1 ... 2.5)	6.9 (4.6 ... 36)	1.3 (1.1 ... 1.5)
MPI-ESM-LR_r1_REMO2009 historical-rcp94	31 (5.3 ... ∞)	1.9 (1.1 ... 2.6)	5.4 (3.4 ... ∞)	1.3 (1.0 ... 1.6)
HadGEM2-ES_r1_RegCM4-7 historical-rcp85	1.9e+5 (4.4 ... ∞)	2.2 (1.2 ... 3.1)	7.5 (3.7 ... ∞)	1.3 (1.0 ... 1.6)

6 Hazard synthesis

For the AugSepTX10x event definition described above, we evaluate the influence of anthropogenic climate change on the events by calculating the probability ratio as well as the change in intensity using both observations and climate models. Models which do not pass the evaluation tests described above are excluded from the analysis. The aim is to synthesise results from models that pass the evaluation along with the observations-based products, to give an overarching attribution statement. Figs. 8 and 9 show the best estimates and confidence intervals for changes in probability and intensity for the observations (blue) and models (red). Before combining them into a synthesised assessment, some other possible sources of error are assessed. (i) Each observational dataset is treated as an equally valid representation of reality but differences, which we call "representation error", arise from different ways of recording that reality. The representation error is estimated from the average scatter of the best estimates (a root-mean-squared error normalised by the degrees of freedom), andis added (in quadrature) to the existing confidence intervals (natural variability) in the observations. This is shown in these figures as white boxes around the light blue bars. The dark blue bar shows the average over the observation-based products. (ii) A term to account for intermodel spread is added (in quadrature) to the natural variability of the models, if the intermodel spread is larger than that expected from natural variability. This is shown in the figures as white boxes around the light red bars. The dark red bar shows the model average, consisting of a weighted mean using the

(uncorrelated) uncertainties due to natural variability plus the term representing intermodel spread (i.e., the inverse square of the white bars). Then observation-based products and models are synthesised into a single result in two ways. Firstly, we neglect common model uncertainties beyond the intermodel spread that is depicted by the model average, and compute the weighted average of models (dark red bar) and observations (dark blue bar): this is indicated by the magenta bar. Secondly, if there is model bias that all models have in common, it cannot be detected from intermodel differences, but may be evident as a misalignment between the group of model results and the group of observational results. If this is the case, the model uncertainty may be larger than that estimated so far. For this reason, we also show the more conservative estimate of an unweighted, direct average of observations (dark red bar) and models (dark blue bar) contributing 50% each, indicated by the white box around the magenta bar in the synthesis figures.

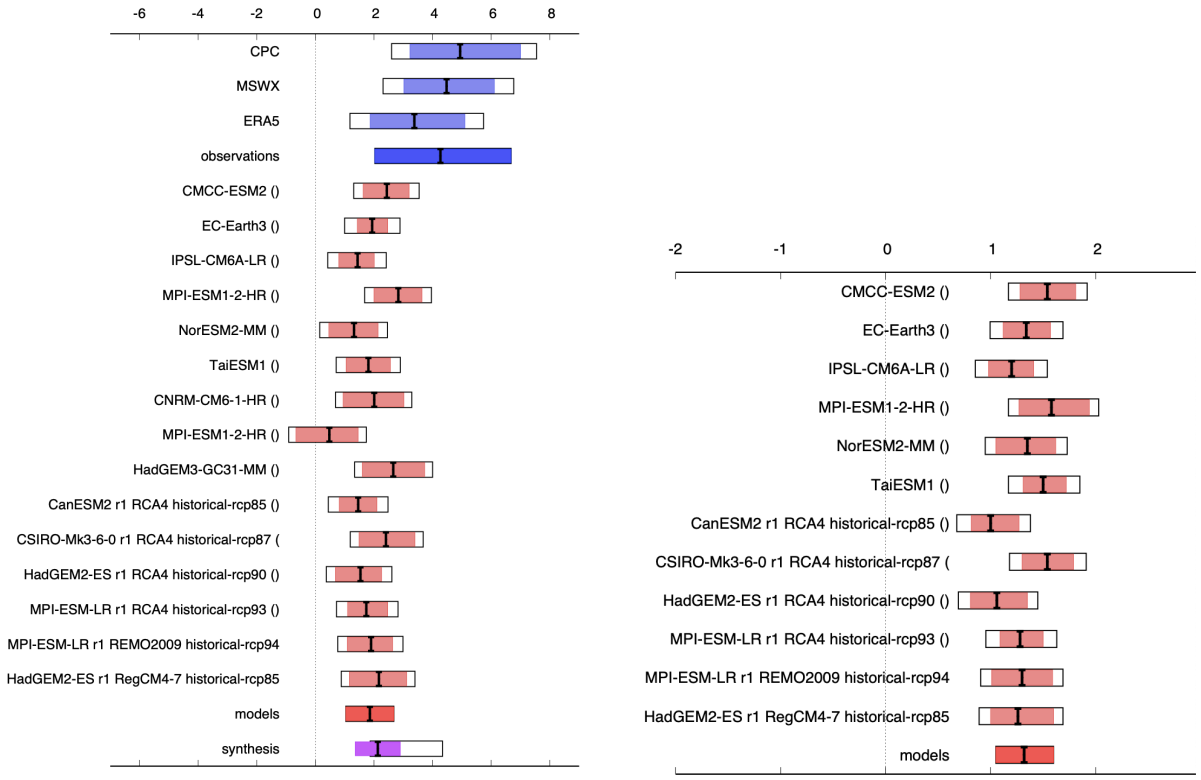

Figure 8: *Synthesis of intensity changes when comparing the magnitudes of the 10-day averaged maximum temperatures over the study region between (a) the current climate and a 1.2°C cooler climate and (b) a 0.8°C warmer (2°C since pre-industrial) climate and the current climate.*

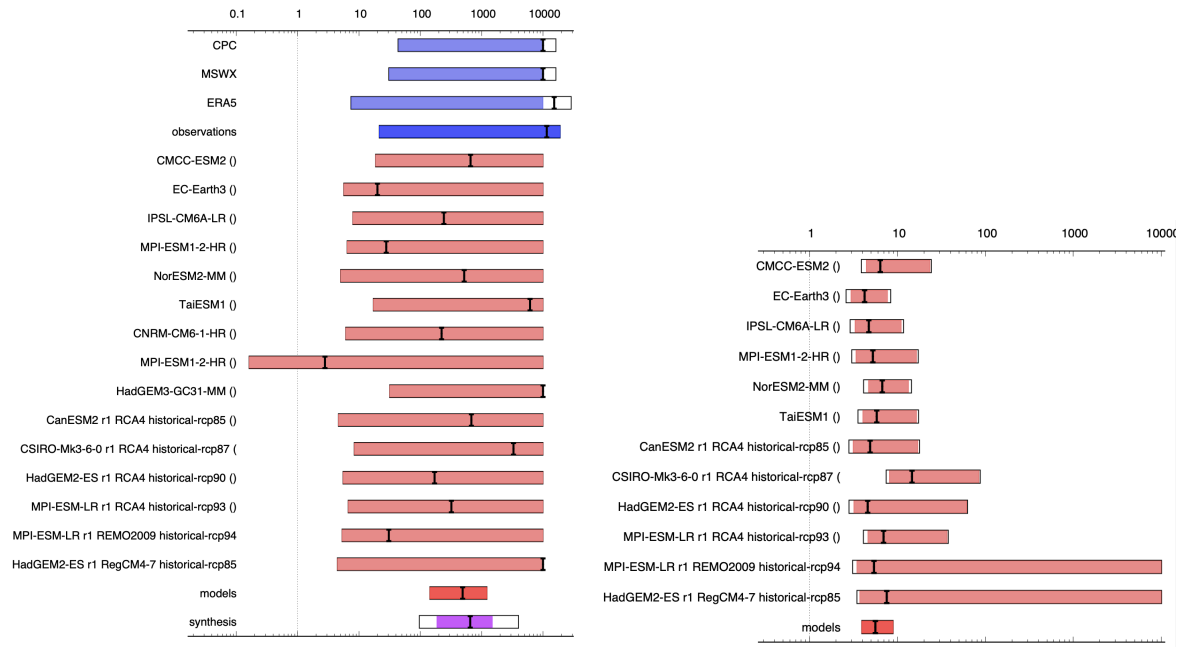

Figure 9. Synthesis of probability ratios when comparing the magnitudes of the 10-day averaged maximum temperatures over the study region between (a) the current climate and a 1.2°C cooler climate and (b) a 0.8°C warmer (2°C since pre-industrial) climate and the current climate. Note that many large values are cut off at 10000 in (a).

Despite differences in the observational time series, the results for the observational analyses are similar; clearly more similar to each other than to the models. It has to be noted that the trend in ERA5 is lower than in CPC and MSWX. This is partly related to the fact that ERA5 has the longest time series. The observational results show somewhat larger trends than the models: the intensity change in the observational average is 3.4 ℃ (2.0 to 6.7 ℃), whereas the model average is 1.9 ℃ (1.0 to 2.7 ℃). This discrepancy could be due to a variety of reasons. This includes the fact that the observational time series is shorter, possible systematic differences between models and observations, and other factors influencing the trend in observations. Consequently, we elect to communicate a range of results between the weighted and unweighted averages of trend in intensity between 1.4 ℃ and 4.3 ℃. For the future, 0.8 ℃ warmer climate, the model best estimate of a change in intensity is about another 1.3℃ with uncertainty ranging from 1.1 ℃ to 1.6 ℃.

Due to the strong trends in such heat events, the probability of such heat events is very low in a 1.2 ℃ cooler climate. As a consequence the probability ratios between the current climate and the 1.2 ℃ the return values are not well defined. Truncating values at 10000 in the synthesis, we obtain a conservative estimate for the probability ratio of at least 100 times. In a future, 0.8 ℃ warmer climate, models estimate that such heat events are another 5.6 (3.9 to 8.9) times more likely.

It is noted that the major barrier to the study of climate change in many regions of South America is still the absence or insufficiency of long time series of observational data, such as Central-West and North Brazil. Most national datasets were created in the 1970s and 1980s, preventing a more comprehensive long-term trend analysis.

7 Vulnerability and exposure

Extreme heat is one of the deadliest natural hazards with thousands of people dying from heat-related causes every year (EM-DAT). However, the true scope of impacts from a heatwave remains unknown until weeks or months after the heatwave has passed, once death certificates have been collected or scientists have had a chance to analyze excess deaths. In many cases, we never know the full extent of the impact to human health since heat-related casualties are often attributed to other causes such as kidney failure or cardiac arrest, when they would not have occurred unless the high temperatures had exacerbated someone's pre-existing condition. However, the link between extremely high temperatures and increased mortality is well-established. Extreme heat also increases morbidity risk, though studies are fewer than studies focused on mortality, excessive temperatures result in including increased usage of emergency health services such as hospitals. (Kravchanko et al. 2013)

Strikingly, across Latin America, a 1℃ increase in daily temperature on hot days (above the 326 studied cities' respective 95th percentile temperature) is associated with a 5.7% higher mortality rate (Kephart et al., 2021). Moreover, heat-related fatalities across South America have soared by 160% from 2000-2004 to 2017-2021 (Hartinger et al., 2023). Mortality risk is notably pronounced in urban centers, where over 87, 62, and 70% of the populations of Brazil, Paraguay, and Bolivia, respectively, reside (Statista, 2022a; Statista, 2022b; Statista, 2022c). This includes São Paulo, Rio de Janeiro, Brasília, Asunción, and a large number of other cities of over 100,000 inhabitants where temperatures regularly exceed 25℃ (Kephart et al., 2021; Green et al., 2019; Bell et al., 2008). High population density, few vegetation and water-based spaces, high levels of air pollution, and inequality are additional risk drivers for mortality and morbidity within cities (Sera et al., 2019). In these urban centers, research suggests that children under the age of 9 and elderly above the age of 65, people with low income, people with limited education, and people with cardiovascular and respiratory diseases are particularly vulnerable to extreme heat (Zhao et al., 2019; Bell et al., 2008). In rural counterparts, agricultural workers are known to be disproportionately impacted due to their high exposure to heat, often linked to kidney disease and failure (Crowe et al., 2015; Jayasumana et al., 2017).

Despite the threat they constitute to humans, heatwaves do not need to result in excess deaths. Simple actions like drinking enough water, finding a cool place to go during the hottest hours of the day, and checking in on your neighbors and relatives can save lives (Singh et al., 2019). It is notably critical for governments to develop heat action plans and early warning systems (EWS) for extreme temperatures. Heat action plans should ensure the continuity or scale-up of key services such as water access, availability of electricity to power cooling devices, and prepare health services to deal with an influx of patients. While available information of the mechanism remains limited, the National Institute of Meteorology of Brazil states that its multi-hazard EWS encompasses extreme heat (Ministry of Environment, 2016). Paraguay, on the other hand, is still only considering the development of a heat EWS (Yglesias-González et al., 2022). Research by Yglesias-González et al. (2022) states that existing heat EWS in South America are city and temperature based only, leaving gaps for rural places while discounting the threats posed by humidity. The same report suggests that there are no heat action plans or equivalent protocols for responding to heat warnings when issued, thus leaving a vastly underutilized window of opportunity for actions to mitigate impacts on vulnerable people.

Meanwhile, people's access to cooling devices, notably fans, has increased in Brazil and Bolivia, which enables some self-protective measures (KIGALI, 2021). However it is crucial to note that during extremely high temperatures, such as near the peak temperatures during this extreme heat event, fans lose efficacy and can begin to have negative health consequences, effectively acting as a

heating device rather than a cooling device. For example, fans can help young, healthy adults cool off when temperatures are 42C and 50% humidity, but will not help older adults. Efficacy further decreases if adequate hydration is not maintained. At higher temperatures and lower humidity such as 47C and 10% humidity, body heating is accelerated across the board, rather than cooling. (Moris et al., 2021) In these situations, skin wetting is a more effective low-cost cooling strategy than fan usage, and tends to be more equitably accessible when coupled with information campaigns to raise awareness about its efficacy.

Cities whose urban planning accounts for extreme heat tend to stay cooler and reduce urban heat island effects which exacerbate the risks associated with heatwaves. Climate change projections for Paraguay are, for instance, expected to markedly increase heat discomfort, known as overheating rates, in urban buildings (Silvero et al., 2019). Reintegrating more nature into the city fabric is key to reducing temperatures (Sera et al., 2019). Adaptation measures must also address underlying issues, as structural vulnerabilities of vast inequality and poverty are significant risk drivers (Yglesias-González et al., 2022). Key systems may also need long-term adaptation to account for increasing demand posed by extreme temperatures both spatially and temporarily as well as higher peak demands, this includes bolstering emergency health services as well as water and electricity services.

Data availability

Almost all data are available via the Climate Explorer.

References

All references are given as hyperlinks in the text.

Appendix

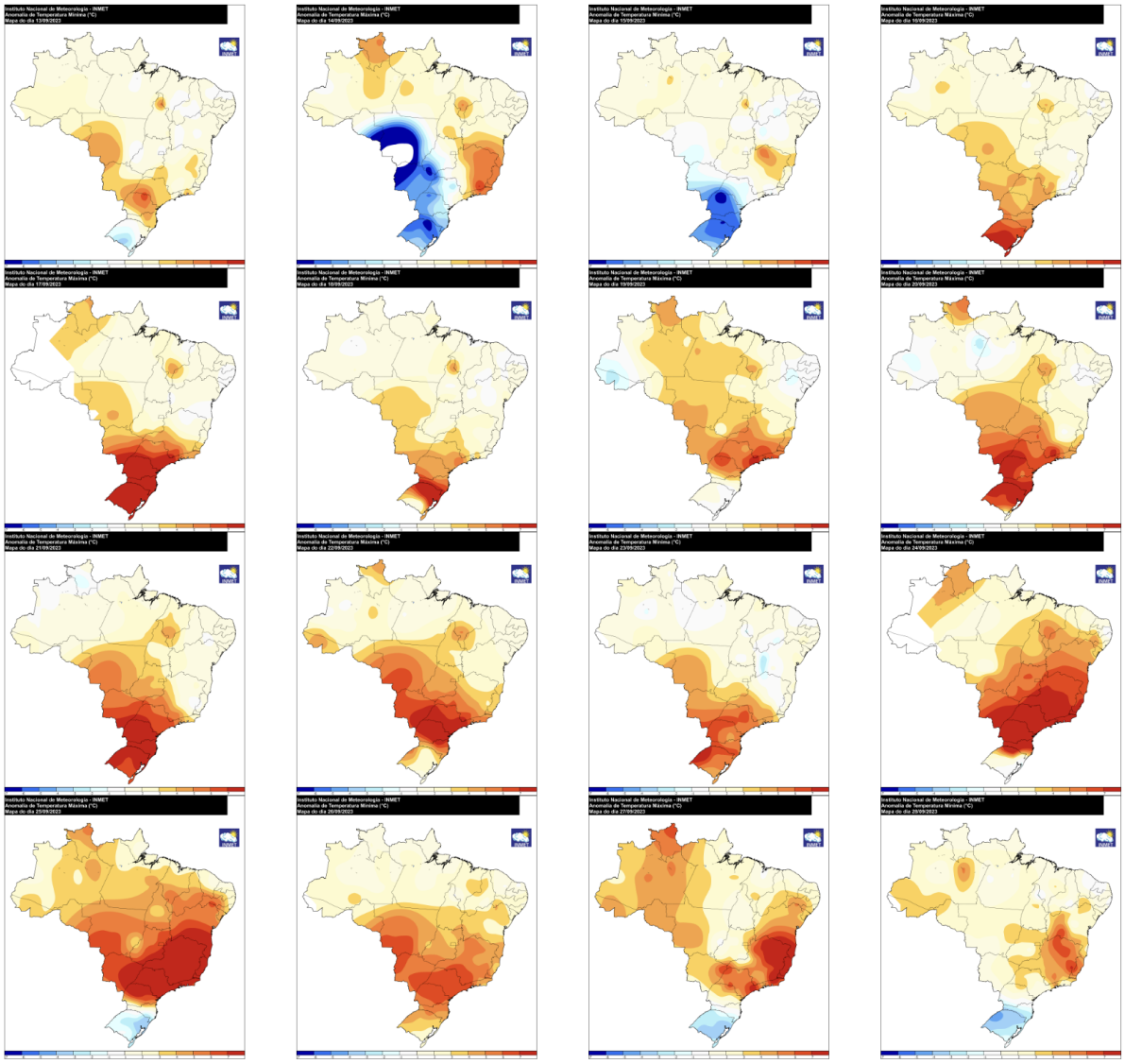

Figure A1. Maps of daily maximum temperature anomalies shown here for 13-28 September 2023, used in this analysis to assess the quality of the observational datasets. Colour scale ranges from -7℃ to +8℃, with -1℃ to +1℃ in white. Source: INMET (Brazilian National Institute of Meteorology).